Biomedical Optics EXPRESS

Evaluation of microsurgical tasks with OCT-guided and/or robot-assisted ophthalmic forceps

Haoran Yu,[1,3] **Jin-Hui Shen,**[2,3]
Rohan J. Shah,[2] **Nabil Simaan,**[1,3] **and Karen M. Joos**[2,3,4,*]

[1]*Mechanical Engineering, Vanderbilt University, 2400 Highland Ave Nashville, TN 37212, USA*
[2]*Vanderbilt Eye Institute, Vanderbilt University 2311 Pierce Avenue Nashville, TN 37232, USA*
[3]*Vanderbilt Initiative in Surgery and Engineering(ViSE), Vanderbilt University 2525 West End Avenue, 6th Floor, Nashville, TN 37203, USA*
[4]*Vanderbilt Biomedical Photonics Laboratories, Vanderbilt University 100 Keck FEL Center, Nashville, TN 37203, USA.*
[*] *karen.joos@vanderbilt.edu*

Abstract: Real-time intraocular optical coherence tomography (OCT) visualization of tissues with surgical feedback can enhance retinal surgery. An intraocular 23-gauge B-mode forward-imaging co-planar OCT-forceps, coupling connectors and algorithms were developed to form a unique ophthalmic surgical robotic system. Approach to the surface of a phantom or goat retina by a manual or robotic-controlled forceps, with and without real-time OCT guidance, was performed. Efficiency of lifting phantom membranes was examined. Placing the co-planar OCT imaging probe internal to the surgical tool reduced instrument shadowing and permitted constant tracking. Robotic assistance together with real-time OCT feedback improved depth perception accuracy. The first-generation integrated OCT-forceps was capable of peeling membrane phantoms despite smooth tips.

OCIS codes: (170.4460) Ophthalmic optics and devices; (150.5758) Robotic and machine control; (170.3880) Medical and biological imaging; (170.4470) Ophthalmology; (170.4500) Optical coherence tomography; (170.4580) Optical diagnostics for medicine.

References and links

1. P.N. Dayani, R. Maldonado, S. Farsiu, and C.A. Toth, "Intraoperative use of handheld spectral domain optical coherence tomography imaging in macular surgery," Retina **29**(10), 1457–1468 (2009).
2. S. Binder, C.I. Falkner-Radler, C. Hauger, H. Matz, and C. Glittenberg, "Feasibility of intrasurgical spectral-domain optical coherence tomography," Retina **31**(7), 1332–1336 (2011).
3. J.P. Ehlers, T. Tam, P.K. Kaiser, D.F. Martin, G.M. Smith, and S.K. Srivastava, "Utility of intraoperative optical coherence tomography during vitrectomy surgery for vitreomacular traction syndrome," Retina **34**(7), 1341–1346 (2014).
4. J.P. Ehlers, D. Xu, P.K. Kaiser, R.P. Singh, and S.K. Srivastava, "Intrasurgical dynamics of macular hole surgery: an assessment of surgery-induced ultrastructural alterations with intraoperative optical coherence tomography," Retina **34**(2), 213–221 (2014).
5. A. Almony, E. Nudleman, G.K. Shah, K.J. Blinder, D.B. Eliott, R.A. Mittra, and A. Tewari, "Techniques, rationale, and outcomes of internal limiting membrane peeling," Retina **32**(5), 877–891 (2012).
6. C. Carpentier, M. Zanolli, L.Wu, G. Sepulveda, M.H. Berrocal, M. Saravia, M. Diaz-Llopis, R. Gallego-Pinazo, L. Filsecker, J.I. Verdaguer-Diaz, R. Milan-Navarro, J.F. Arevalo, and M. Maia, "Residual internal limiting membrane after epiretinal membrane peeling: results of the Pan-American Collaborative Retina Study Group," Retina **33**(10), 2026–2031 (2013).

#227007 - $15.00 USD Received 17 Nov 2014; accepted 22 Dec 2014; published 9 Jan 2015

7. C. Lee, K. Kim, S. Han, S. Kim, J.H. Lee, H.K. Kim, C. Kim, W. Jung, and J. Kim, "Stimulated penetrating keratoplasty using real-time virtual intraoperative surgical optical coherence tomography," J. Biomed. Opt. **19**(3), 30502 (2014).
8. J.P. Ehlers, S.A. McNutt, P.K. Kaiser, and S.K. Srivastava, "Contrast-enhanced intraoperative optical coherence tomography," Br. J. Ophthalmol. **97**(11), 1384–1386 (2013).
9. P. Hahn, J. Migacz, R. O'Donnell, S. Day, A. Lee, P. Lin, R. Vann, A. Kuo, S. Fekrat, P. Mruthyunjaya, E.A. Postel, J.A. Izatt, and C.A. Toth, "Preclinical evaluation and intraoperative human retinal imaging with a high-resolution microscope-integrated spectral domain optical coherence tomography device," Retina **33(**7), 1328–1337 (2013).
10. Y.K. Tao, S.K. Srivastava, and J.P. Ehlers, "Microscope-integrated intraoperative OCT with electrically tunable focus and heads-up display for imaging of ophthalmic surgical maneuvers," Biomed. Opt. Express **5**(6), 1877–1885 (2014).
11. J.P. Ehlers, S.K. Srivastava, D. Feiler, A.I. Noonan, A.M. Rollins AM, and Y.K. Tao, "Integrative advances for OCT-guided ophthalmic surgery and intraoperative OCT: microscope integration, surgical instrumentation, and heads-up display surgeon feedback," PLoS One **9**(8), e105224-1-10 (2014).
12. J.U. Kang, Y. Huang, K. Zhang, Z. Ibrahim, J. Cha, W.P.A. Lee, G. Brandacher, and P.L. Gehlbach, "Real-time three-dimensional Fourier-domain optical coherence tomography video image guided microsurgeries," J. Biomed. Opt. **17**(8), 081403-1-6 (2012).
13. M.F. Kraus, J.J. Liu, J. Schottenhamml, C.L. Chen, A. Budai, L. Branchini, T. Ko, H. Ishikawa, G. Wollstein, J. Schuman, J.S. Duker, J.G. Fujimoto, and J. Hornegger, "Quantitative 3D-OCT motion correction with tilt and illumination correction, robust similarity measure and regularization," Biomed. Opt. Express **5(**8), 2591–2613 (2014).
14. P. Hahn, J. Migacz, R. O'Connell, J.A. Izatt, and C.A. Toth, "Unprocessed real-time imaging of vitreoretinal surgical maneuvers using a microscope-integrated spectral-domain optical coherence tomography system," Graefes Arch. Clin. Exp. Ophthalmol. **251(**1), 213–220 (2013).
15. J.P. Ehlers, Y.K. Tao, S. Farsiu, R. Maldonado, J.A. Izatt, and C.A. Toth, "Integration of a spectral domain optical coherence tomography system into a surgical microscope for intraoperative imaging," Invest. Ophthalmol. Vis. Sci. **52**(6), 3153–3159 (2011).
16. P. Hahn, J. Migacz, R. O'Connell, R.S. Maldonado, J.A. Izatt, and C.A. Toth, "The use of optical coherence tomography in intraoperative ophthalmic imaging," Ophthalmic Surg. Lasers Imaging **42(**Suppl), S85–S94 (2011).
17. J.P. Ehlers, Y.K. Tao, S. Farsiu, R. Maldonado, J.A. Izatt, and C.A. Toth, "Visualization of real-time intraoperative maneuvers with a microscope-mounted spectral domain optical coherence tomography system," Retina **33**(1), 232–236 (2013).
18. M.T. Witmer, G. Parlitsis , S. Patel, and S. Kiss, "Comparison of ultra-widefield fluorescein angiography with the Heidelberg Spectralis(Ⓡ) noncontact ultra-widefield module versus the Optos(Ⓡ) Optomap(Ⓡ)," Clin. Ophthalmol. **7**, 389–394 (2013).
19. D.E. Croft, J. Van Hemert, C.C. Wykoff, D. Clifton, M. Verhoek, A. Fleming, and D.M. Brown, "Precise montaging and metric quantification of retinal surface area from ultra-widefield fundus photography and fluorescein angiography," Ophthalmic Surg. Lasers Imaging Retina **45(**4), 312–317 (2014).
20. M. Balicki, J. H. Han, I. Iordachita, P. Gehlbach, J. Handa, R. Taylor, and J. Kang, "Single fiber optical coherence tomography microsurgical instruments for computer and robot-assisted retinal surgery," in *Medical Image Computing and Computer-Assisted Intervention MICCAI 2009*, G-Z. Yang, D.R. Hawkes, D. Rueckert, A. Noble, C. Taylor, eds., (Springer, 2009), pp. 108–115.
21. S. W. Yang, M. Balicki, R. A. MacLachlan, X. Liu, J. U. Kang, R. H. Taylor, and C. M. Riviere, "Optical coherence tomography scanning with a handheld vitreoretinal micromanipulator," in *Proceedings Annual International Conference of the IEEE Engineering in Medicine and Biology Society*, (IEEE, 2012), pp. 948–951.
22. C. Song, D. Y. Park, P. L. Gehlbach, S. J. Park, J. U. Kang, "Fiber-optic OCT sensor guided "SMART" microforceps for microsurgery," Biomed. Opt. Express **4**(7), 1045–1050 (2013).
23. K.M. Joos and J.H. Shen, "Miniature real-time intraoperative forward-imaging optical coherence tomography probe," Biomed. Opt. Express **4**(8), 1342–1350 (2013).
24. Z. Li, J. H. Shen, J. A. Kozub, R. Prasad, P. Lu, and K. M. Joos, "Miniature forward-imaging B-scan optical coherence tomography probe to guide real-time laser ablation," Lasers Surg. Med. **46**(3), 193–202 (2014).
25. K. W. Grace, P. Jensen, E. J. Colgate and M. Glucksberg, "Teleoperation for ophthalmic surgery: From the Eye Robot to feature extracting force feedback," Automatica **16**(4),293–310 (1998).
26. H. Das, H. Zak, J. Johnson, J. Crouch and D. Frambach, "Evaluation of a telerobotic system to assist surgeons in microsurgery," Computer Aided Surg. **4**(1), 15–25 (1999).
27. R. Taylor, P. Jensen, L. Whitcomb, A. Barnes, R. Kumar, D. Stoianovici, P. Gupta, Z. Wang, E. deJuan, and L. Kavoussi, "Steady-hand robotic system for microsurgical augmentation," Int. J. Robotics Res. **18**(12), 1201–1210 (1999).
28. C. N. Riviere, W. T. Ang, and P. K. Khosla, "Toward active tremor canceling in handheld microsurgical instruments," IEEE Trans. Robotics Automation **19(**5), 793–800 (2003).
29. A. Bettini, S. Lang, A. Okamura, G. Hage, "Vision assisted control for manipulation using virtual fixtures:

#227007 - $15.00 USD Received 17 Nov 2014; accepted 22 Dec 2014; published 9 Jan 2015

experiments at macro and micro scales," in *Proceedings of 2002 IEEE International Conference on Robotics and Automation*, (IEEE, 2002), pp. 3354–3361.
30. B. C. Becker, R. A. Maclachlan, L. A. Lobes, G. D. Hager, C. N. Riviere, "Vision-based control of a handheld surgical micromanipulator with virtual fixtures," IEEE Trans. Robotics **29**(3), 674–683 (2013).
31. T. Ueta, Y. Yamaguchi, Y. Shirakawa, T. Nakano, R. Ideta, Y. Noda, A. Morita, R. Mochizuki, N. Sugita, M. Mitsuishi and Y. Tamaki, "Robot-assisted vitreoretinal surgery: development of a prototype and feasibility studies in an animal model," Ophthalmology **116**(8), 1538–1543 (2009).
32. W. Wei, R. E. Goldman, H. F. Fine, S. Chang, and N. Simaan, "Performance evaluation for multi-arm manipulation of hollow suspended organs," IEEE Trans. Robotics **25**(1), 147–157 (2009).
33. W. Wei, C. Popplewell, H. Fine, S. Chang, and N. Simaan, "Enabling technology for micro-vascular stenting in ophthalmic surgery," ASME J. Med. Devices **4**(2), 014503 (2010).
34. W. Wei and N. Simaan, "Modeling, force sensing, and control of flexible cannulas for microstent delivery," J. Dynamic Syst., Measurement, Control **134**(4), 041004 (2012).
35. B. C. Becker, S. Voros, L. A. Lobes, J. T. Handa, G. D. Hager, and C. N. Riviere, "Retinal vessel cannulation with an image-guided handheld robot," in *Proceeding of Annual International Conference of the IEEE Engineering in Medicine and Biology Society*, (IEEE, 2010), pp. 5420–5423.
36. Y. Noda, Y. Ida, S. Tanaka, T. Toyama, M.F. Roggia, Y. Tamaki, N. Sugita, M. Mitsuishi, and T. Ueta,"Impact of robotic assistance on precision of vitreoretinal surgical procedures," PLoS One **8**(1), e54116 (2013).
37. X. Liu, M. Balicki, R. H. Taylor, J. U. Kang, "Towards automatic calibration of Fourier-domain OCT for robot-assisted vitreoretinal surgery," Opt. Express **18**(23), 24331–24343 (2010).
38. X. Liu, M. Balicki, R. H. Taylor, and J. U. Kang, "Automatic online spectral calibration of Fourier-domain OCT for robotic surgery," Proc SPIE **7890**, (2011).
39. J.R. Wilkins, C.A. Puliafito, M.R. Hee, J.S. Duker, E. Reichel, J.G. Coker, J.S. Schuman, E.A. Swanson, and J.G. Fujimoto, "Characterization of epiretinal membranes using optical coherence tomography," Ophthalmology **103**(12), 2142–1251 (1996).
40. S. S. Gurbani, P. Wilkening, M. Zhao, B. Gonenc, G. W. Cheon, I. I. Iordachita, W. Chien, R. H. Taylor, J. K. Niparko, and J. U. Kang, "Robot-assisted three-dimensional registration for cochlear implant surgery using a common-path swept-source optical coherence tomography probe," J. Biomed. Opt. **19**(5), 057004 (2014).
41. H. Yu, J.-H. Shen, K. M. Joos, and N. Simaan, "Design, calibration and preliminary testing of a robotic telemanipulator for OCT guided retinal surgery," in *Proceedings of IEEE International Conference on Robotics and Automation*, (IEEE 2013), pp. 225–231.
42. M. N. Iyer and D. P. Han, "An eye model for practicing vitreoretinal membrane peeling," Arch. Ophthalmol. **124**(1), 108–110 (2006).
43. J. P. Ehlers, M. P. Ohr, P. K. Kaiser, and S. K. Srivastava, "Novel microarchitectural dynamics in rhegmatogenous retinal detachments identified with intraoperative optical coherence tomography," Retina **33**(7), 1428–1434 (2013).
44. Y. Huang and J.U. Kang, "Real-time reference A-line subtraction and saturation artifact removal using graphics processing unit for high-frame-rate Fourier-domain optical coherence tomography video imaging," Opt. Eng. **51**(7), 073203-1-5 (2012).

1. Introduction

Optical coherence tomography (OCT) has become widely used as an important diagnostic and surgical pre-planning tool in ophthalmology. This imaging modality provides valuable depth information of various disease processes within the retina. Peri-operative scans, including handheld or microscope-coupled systems, produce information regarding the extent and location of vitreomacular traction [1–3], macular holes [1, 2, 4], and visually significant epiretinal membranes including characterization of membrane edges [1, 2, 5, 6]. Improved real-time intraoperative location of these edges would improve success rates of complete membrane removal and would reduce the use of potentially toxic dyes to visualize the membranes. Dayani, *et al.* published the first approach to using intraoperative OCT imaging with a handheld external device to evaluate the retina prior to incision, and to evaluate retinal changes and procedure completeness during planned interruptions of the surgical procedures [1]. Binder, *et al.* performed a foundational study with an external microscope-mounted OCT operating room system to image retinal changes immediately following surgical manipulations [2]. Several other surgical microscope-mounted OCT systems with heads-up displays are being developed to provide real-time visualization in the operating room for anterior segment [7], and for posterior

#227007 - $15.00 USD Received 17 Nov 2014; accepted 22 Dec 2014; published 9 Jan 2015

segment [2–4, 8–11] surgeries. Improvements have been made to permit imaging during a procedure [3, 4, 7, 10, 11]. Three-dimensional surgical systems are also being developed [10–12]. Artifacts of motion, variable illumination, and tilt affect 3D-OCT images necessitating ongoing post-processing algorithm developments for static clinical 3D-OCT images [13]. Surgical limitations have included the complete blockage of the underlying retinal image by shadowing from standard stainless steel intraocular instruments, as well as problematic tracking of instrument movements within the OCT image, thus reducing useful real-time surgical guidance [14–17]. A forward-viewing intraocular surgical B-scan OCT probe co-planar with an intraocular instrument would provide a mechanism to bypass these issues and directly view the tissue structures in real time. In addition, an intraocular probe would bypass media obstructions including corneal opacities, miosis, and lenticular opacities that degrade an external OCT image. A miniature probe would permit cross-sectional images of epiretinal membranes and their edges thus enabling surgeons to scan the retina to determine if the membrane peeling was satisfactorily completed prior to removing the instruments. Besides imaging macular pathology, an intraocular probe would be able to transmit direct images of peripheral membranes and lesions without the distortions inherent in peripheral images with external OCT systems [18, 19].

Balicki, *et al.*, was first to demonstrate an A-mode single fiber common-path OCT probe combined with a 25-gauge pick for retinal applications [20]. However, the entire instrument must move back and forth inside the eye only 1.6 mm above the retinal surface to produce two-dimensional B-scan images, while using external metrology for tracking the probe tip movement [20, 21]. This fiberoptic common-path OCT was coupled to the side of a modified commercial forceps to provide A-scan precision depth sensing [22]. Joos and Shen developed a 25-gauge (0.51 mm outer diameter) hand-held forward-imaging B-scan OCT probe and demonstrated its feasibility for ophthalmic examination including retinal tissue [23]. The miniature probe passes through the now standard 23-gauge (0.64 mm) and 25-gauge (0.51 mm) surgical instrument ports to permit real-time intraocular imaging. Scanning occurs within the probe and does not require an external means for moving the probe in order to obtain B-mode images [23]. Li, *et al.*, recently demonstrated that this OCT probe when combined with a laser was capable of monitoring real-time incising of ocular tissues including retina to avoid cutting the retinal pigment epithelium in *ex vivo* attached retinas [24]. The probe is a manually controlled surgical instrument, but adding robotic assistance also may expand its capability for future surgical maneuvers such as subretinal surgery, targeted gene therapy, or retinal microvascular procedures.

Robot-assisted ophthalmic surgery has been investigated to enhance surgical accuracy while overcoming physiological tremor and permitting the development of new tissue layer or cellular micro-techniques to treat ocular conditions. Initial telemanipulation control and feature extraction improved accuracy in sub-retinal injections [25]. An alternative wire-actuated telemanipulation robotic slave was designed by Das, *et al.*, for assistance in experimental ophthalmic surgery [26]. Instead of using telemanipulated robots, Taylor, *et al.*, used the concept of hands-on or cooperative manipulation of a steady-hand robot for micro-manipulation [27]. Riviere, *et al.* also reported instrument tremor reduction with robotic assistance [28]. With an endoscope, Bettini, *et al.*, demonstrated the utility of robotic vision-guided control laws that enforced motion constraints and/or provided corrective assistive motions to guide users in micromanipulation tasks [29]. An extension of this approach recently was demonstrated in a hand-held tremor-cancelling robot [30]. Ueta, *et al.*, built a prototype robot and demonstrated feasibility for pointing, retinal vessel sheathotomy, and retinal microvascular injection in cadaver porcine eyes [31]. A dual-arm robotic system capable of both orbital and intraocular manipulation was proposed by Wei, *et al.* [32]. This system was mathematically modeled for four modes including: movement of the eye using external robotic tools; movement of intraocular robotic instruments within a stabilized eye; maintenance of intraocular instrument positions

#227007 - $15.00 USD Received 17 Nov 2014; accepted 22 Dec 2014; published 9 Jan 2015

relative to the retina during controlled eye movements; and simultaneous movements of the eye and intraocular instruments. This group demonstrated the feasibility of micro-stent deployment in a chick chorioallantoic membrane vascular model [33], and subsequently demonstrated an algorithm for force sensing and telemanipulation assistance for microvascular stent deployment [34]. Improved vessel cannulation with robotic assistance was also found by Becker, *et al.* [35]. Noda, *et al.*, reported telerobotic assistance improved lateral movement accuracy, tool stability, and depth perception accuracy in a phantom eye model [36]. Improvements have been made in tremor cancellation, precision pointing, force feedback, and virtual fixtures.

In addition, Yu, *et al.*, enhanced a telemanipulated system design by incorporating constrained telemanipulation algorithms for theoretical intraocular manipulation of a probe with a single-arm robotic system [41]. The initial design of a forceps integrated into the intraocular forward-imaging B-scan OCT probe is described in this paper with evaluation of manual and robotic-assisted tasks upon a gelatin phantom and *ex vivo* retinal tissue. Performances of it and a standard retinal forceps without OCT guidance are compared. The evaluation of robot assistance combined with or without B-scan OCT feedback for retinal microsurgery has not been previously published.

2. OCT-forceps probe design and robotic ophthalmic system design

2.1. Combined forward-imaging B-scan OCT probe and forceps design with technical performance

A miniature B-scan OCT probe uniquely combined with an ophthalmic surgical forceps was designed with the probe positioned within the forceps rather than a forceps positioned within or adjacent to the OCT probe (Fig. 1(a) and 1(b)). The detailed structure of just the miniature 0.51 mm-diameter intraocular OCT probe was previously described [23]. Briefly, this probe has a cylindrical body that is 90 to 100 mm long with a handpiece 12.7 mm in diameter and disposable 25-gauge extra-thin-wall probe tip (outer diameter = 0.51 mm, wall thickness = 70 μm, and length = 34 mm beyond the end of the handpiece). An electromagnetic linkage is embedded within the handpiece, to drive the 125 μm single-mode fiber optic actuator within the 25-gauge probe tip. The fiber can easily scan laterally up to 30Hz. The fiber scanning frequency was matched to the acquisition rate of an available commercial VHR spectral-domain optical coherence tomography (SDOCT) system (870 nm, Bioptigen, Inc. Morrisville, NC) which permitted real-time viewing with highest resolution B-scan generation at 5Hz with 2000 A-scan lines per image. A sealed 0.35 mm diameter, 0.5 mm thick, $<$ 1/4 pitch, 0.95 numerical aperture GRIN lens (Go!Foton, Somerset, NJ) within the probe protected the fiber scanner and focused the scanning beam at the working distance 3 to 4 mm away from the probe. The axial resolution was $4-6\mu m$ and the lateral resolution was $25-35\mu m$ centrally and $32-45\mu m$ at the scanning edge periphery [23].

To produce the coupled forceps, the front portion of the 25-gauge stainless steel tube (SST) was cut to form a forceps with 3.5 mm long tips, and positioned so that the OCT beam scan intersected both tips. The forceps tips were fabricated to be aligned with the cross-sectional center of the probe, and located 3.5 mm distal to the OCT tip to be at the best focal point position. The forceps tips were mechanically aligned to match the scanning beam. A 23-gauge extra-thin wall SST was used to slide up and down the outside of the 25-gauge tube to cause opening and closure of the gripper manually (Fig. 1(a)). A manual gripper actuator was concentrically assembled around the OCT probe handpiece and attached to the 23-gauge tube to open/close the forceps (Fig. 1(b)). This actuator was designed and fabricated from a 0.005" thick stainless steel sheet. The length of the handles was approximately 42 mm with an actuation distance of approximately 1.5 mm. The distal handles were attached to the OCT handpiece with a hoop design. The proximal handles were attached to a plastic ring which was connected to the 23-

#227007 - $15.00 USD Received 17 Nov 2014; accepted 22 Dec 2014; published 9 Jan 2015

gauge extra-thin wall SST on the forceps to actuate gripper closure. The OCT forceps may be used as either a hand-held instrument or integrated within a robotic system. One frame of the OCT image appearance of the forceps tips is illustrated in Fig. 1(c) with real-time unprocessed OCT imaging of the forceps' tips closing and opening demonstrated (Media 1).

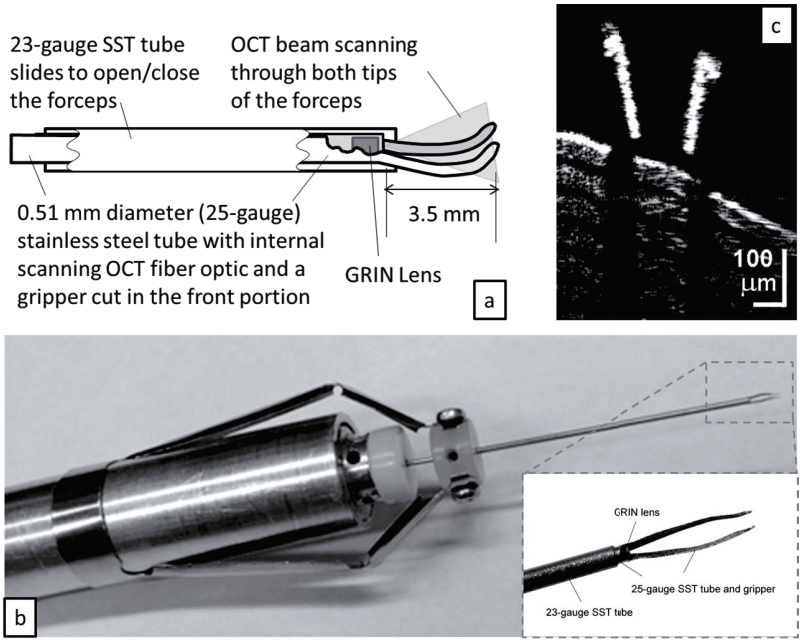

Fig. 1. OCT-forceps probe design with OCT images of the probe's tips. (a) Drawing of the OCT-forceps probe design with an internal 0.51 mm diameter (25-gauge) stainless steel tube (SST) with embedded scanning OCT fiber optic and a gripper cut in the front portion. An external 23-gauge SST slides to open/close the forceps. The OCT beam scans through both tips of the forceps. (b) An external manual hand piece actuator causes the external 23-gauge SST tube to slide which opens/closes the forceps. (c) The unprocessed OCT image appearance of the forceps' tips is illustrated with real-time OCT imaging of the forceps' tips closing and opening demonstrated (Media 1).

Because external OCT systems produce marked peripheral distortions with wide angle lenses [18,19], knowledge of the maximal tilt angle is important. The eye has an oblate spheroid shape and the intraocular reach of all intraocular instruments are minimally constrained with a flexible pars plana sclerotomy. In addition, the usual placement of two flexible sclerotomy entry ports and performance of indentation of the peripheral retina will minimize tilt relative to the retinal surface. However, a region of the retina may be imaged at an angle using this probe. We tested the OCT probe in conditions whereby the probe's imaging axis was at an angle θ from the image surface normal as the probe was tilted as shown in Fig. 2(a). The probe's tilting axis was perpendicular to the probe's scanning plane. Figures 2(b) and 2(c) show the OCT images of a cellophane tape roll with different θ angles when scanning longitudinally. The probe achieved the best scanning quality when the probe was -10° to the surface plane. The OCT image quality deteriorates as the probe tilted in both positive and negative directions. Beyond 30°, the image quality is no longer usable for guiding the surgery. Figures 2(b) and 2(c), show that the imaging surface is not flat. This distortion stems from the intrinsic lens and scanning parameters of the probe. A real-time algorithm to calibrate these intrinsic parameters in order to correct image distortion is currently being developed.

#227007 - $15.00 USD Received 17 Nov 2014; accepted 22 Dec 2014; published 9 Jan 2015

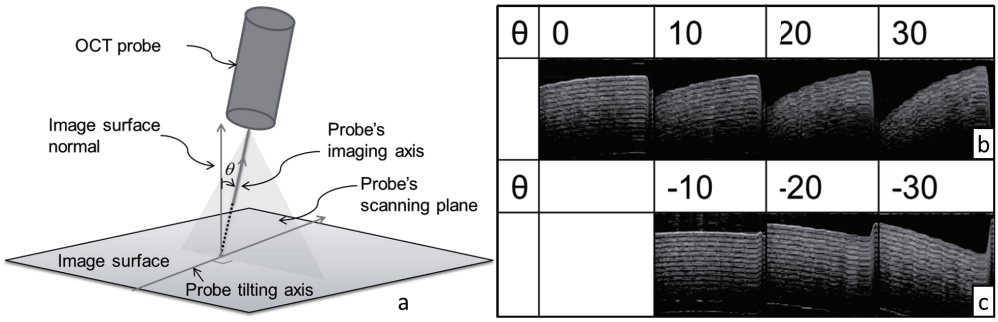

Fig. 2. Diagram and images of a cellophane tape roll for different OCT tilts. (a) Diagram of a positive angle θ tilt from the normal direction. (b) Images produced when tilting longitudinally to the OCT scanning beam in (+) angle θ direction according to the right hand rule about the probe tilting axis. (c) Images produced when tilting in (-) θ direction according to the right hand rule about the probe tilting axis.

2.2. Robotic setup and operation

The combined B-scan OCT-guided robotic concept for ophthalmic microsurgery was previously theoretically described [41]. Figure 3(a) delineates the actual seven Degree of Freedom (DoF) modular robot arm composed from a custom-designed six DoF Stewart-Gough parallel robot and a cam-actuated surgical gripper. The parallel robot is driven by a seven DoF haptic master device (Force Dimension Omega 7 ®, Nyon, Switzerland). This device tracks and transmits the surgeon's hand movements along with the variable opening and closing angle of the 7^{th} DoF controlling the gripper's desired grasping motion. To use the robotic system, the surgeon sat in front of the robot and held the master device and activated a foot pedal to engage and maintain telemanipulation. A scale of 0.02 was used for converting translational hand movements to commanded robot-assisted forceps movements. In the current study, rotational movements of the forceps along its center axis were not scaled, but will be added in the future.

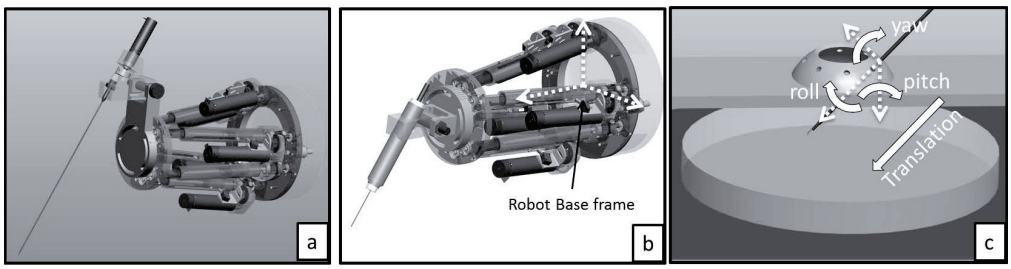

Fig. 3. Robotic design and layout. (a) A 7 Degree of Freedom (DOF) robot was used in this experiment with 6 DOF parallel robot and 1 DOF gripper. (b) The 6 DOF parallel robot also controlled the OCT-forceps probe. (c) Demonstration of the remote center of motion (RCM) located at the sclerotomy in the phantom model eye.

To ensure that the instrument's motions respected the limitations of operating through a sclerotomy, a remote center of motion (RCM) constraint was integrated into the telemanipulation framework [32,41]. Initially, the surgeon telemanipulated the pre-registered gripper tip mounted on the robotic arm to digitize the RCM point in the robot base frame. The location of the RCM point was saved in the high-level control algorithm. After digitizing the sclerotomy, the surgeon

#227007 - $15.00 USD Received 17 Nov 2014; accepted 22 Dec 2014; published 9 Jan 2015

guided the robot to insert the gripper through the sclerotomy. During this phase, the telemanipulation was carefully performed without imposing RCM constraints. After the robot-assisted gripper was inside the eye model, the RCM constraints were enabled. The assisted telemanipulation automatically maintained the scleral constraints while allowing the surgical instrument to move with four degrees of freedom (pitch/yaw and translate/roll along the longitudinal axis of the tool) (Fig. 3(c)).

3. Experimental design

The two tasks designed for evaluating the performance of manual manipulation and robot-assisted telemanipulation were: 1) controlled approach and touch of the forceps' tips to a surface, and 2) peeling of a surface membrane. In the first task, the surgeon was asked to bring the surgical forceps towards the surface of a gelatin model (20 g Knox Gelatine powder (Kraft Foods Global, Inc., Northfield, IL)), and 60 g Coffee-mate (Nestle USA, Glendale, CA) in 250 ml hot water) or the surface of a goat *ex vivo* retina. The goal was to touch the gripper tip to the surface with minimal penetration into the phantom or retinal tissue. Although the OCT probe was capable of imaging retina through vitreous in an intact cadaver goat eye as shown in Fig. 5(a), 5(b) and 5(c), we chose the *ex vivo* model to enable side-view recording of the instrument touching the surface. For the membrane peeling task, the surgeon lifted a uniform phantom membrane which was created using New-Skin Liquid Bandage (Medtech Products, Inc., Irvington, NY) placed on the gelatin surface based upon the protocol of Iyer, *et al.* [42]. The thickness of this phantom membrane was approximately 10 μm. This phantom membrane was thinner than an epiretinal membrane averaging about 61 μm [39]. However, it was greater than the average internal limiting membrane thickness of 2.5 μm. Formation of artificial membranes upon cadaver goat retina was not uniform as seen in Fig. 5(d), 5(e) and 5(f), with variability ranging from a thin coating Fig. 5(d), to non-adherence due to retinal surface moisture Fig. 5(e), to contraction of the retina surface Fig. 5(f). Therefore, this model was not used to compare the techniques since nonuniform membrane formation was a confounding variable.

3.1. Experimental layout and experimental conditions

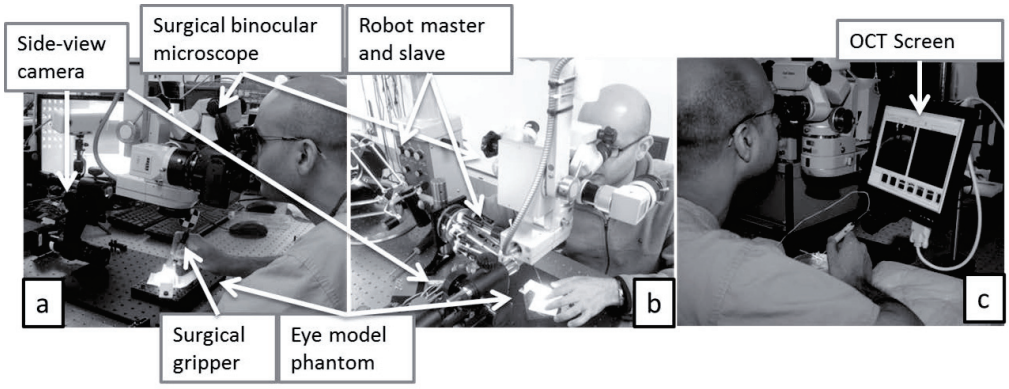

Fig. 4. Experimental layout for manual and robot-assisted tasks. (a) For manual manipulation, the surgeon held an ophthalmic forceps or B-scan OCT-forceps and manipulated the forceps through a mockup sclerotomy constraint above the gelatin retinal phantom. (b) For robotic manipulation, the surgeon held the robot master device and controlled the slave robot to manipulate a customized ophthalmic forceps. (c) Layout with a small side-view OCT screen to improve visualization of real-time OCT feedback.

#227007 - $15.00 USD Received 17 Nov 2014; accepted 22 Dec 2014; published 9 Jan 2015

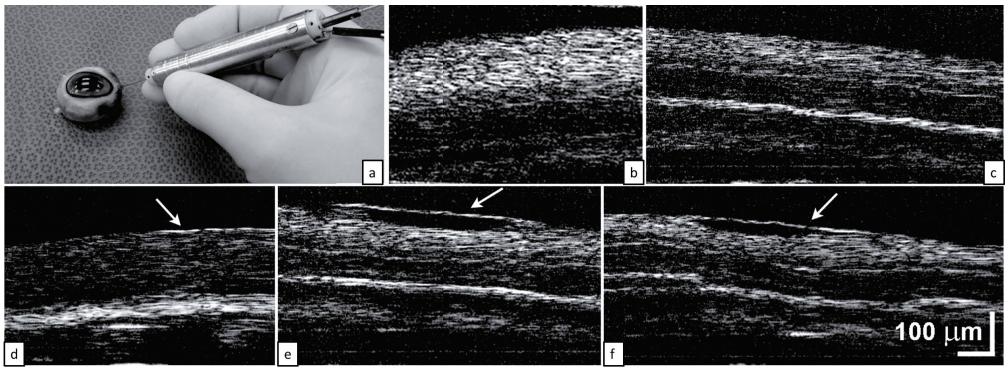

Fig. 5. (a-c) The OCT probe with approximately 2mm scan length is capable of imaging retina through vitreous in an intact cadaver goat eye. (d-f) *Ex vivo* goat retina was used to enable application of artificial membranes. Nonuniform (d) tight adherence, (e) loose adherence, or (f) retinal contraction developed. Scale bars indicate the length of the images.

Figure 4 shows the experimental setup for both manual manipulation and robot-assisted telemanipulation. The phantom retinal platform consisted of a plastic-molded sclerotomy and the gelatin surface (Fig. 3 (c)). A side-viewing microscope (Omano E-ZVU/V-15 Digital Microscope, Japan) with attached camera (Dragonfly 2 ®, Point Grey Research Inc., Richmond, Canada) recorded an external video of the gripper tip's motion. These images were not visible to the surgeon, and were used for post-processing analysis of the forceps' motions.

When performing the manual tasks (Fig. 4(a)), the surgeon held either a standard Grieshaber Revolution DSP MaxGrip intraocular forceps (Alcon, Fort Worth, TX) or the 23-gauge combined B-scan OCT-forceps. During the robot-assisted modes (Fig. 4(b)), the surgeon held the master device and activated a foot pedal to enable the robotic telemanipulation coupling. When real-time OCT feedback was introduced into the experimental conditions, the surgeon worked with two visual inputs: 1) the surgical binocular microscope and 2) a large distant real-time OCT video screen. Repeated redirection of the eyes from the binocular microscope to visualize the OCT images can significantly diminish hand stability. Therefore, to reduce the impact of this distraction, a small 7" screen (SMART USB Monitor, Model: DS-70U, DoubleSight Displays, Costa Mesa, CA), which displayed the real-time OCT images, was positioned adjacent to the binocular microscope (Fig. 4(c)). Less ocular movement was required to view this small screen for real-time OCT feedback.

Table 1 lists the experimental conditions with the approaching task evaluated with both the gelatin model and goat *ex vivo* retinas, and the membrane peeling task evaluated with the gelatin model. Membrane peeling with the *ex vivo* retinas was not performed due to difficulty in replicating identical membranes on this tissue (Fig. 5(d), 5(e) and 5(f)). The gelatin phantom approach experimental conditions were: (A) manual surgical forceps, (B) robot-assisted forceps, (C) manual B-scan OCT-forceps, (D) robot-assisted B-scan OCT-forceps, and (E) manual B-scan OCT-forceps with OCT-image side screen. The *ex vivo* retinal surface approach experimental conditions were:(F) manual surgical forceps, (G) robot-assisted forceps, (H) manual B-scan OCT-forceps, (I) robot-assisted B-scan OCT-forceps, and (J) manual B-scan OCT-forceps with OCT-image side screen. The phantom membrane peeling conditions were: (K) manual surgical forceps, (L) robot-assisted forceps, and (M) manual B-scan OCT-forceps with OCT-image side screen. The effect of the small adjacent monitor regarding OCT feedback was determined by comparing conditions (E) to (C) and (J) to (H).

#227007 - $15.00 USD Received 17 Nov 2014; accepted 22 Dec 2014; published 9 Jan 2015

Table 1. Experimental models and conditions used.

Task	Exp. #	Model	Manual	Robot-assisted	OCT Feedback	OCT Side Screen
Approach	A	Gelatin	✓			
	B	Gelatin		✓		
	C	Gelatin	✓		✓	
	D	Gelatin		✓	✓	
	E	Gelatin	✓		✓	✓
Approach	F	Goat retina	✓			
	G	Goat retina		✓		
	H	Goat retina	✓		✓	
	I	Goat retina		✓	✓	
	J	Goat retina	✓		✓	✓
Peeling	K	Gelatin	✓			
	L	Gelatin		✓		
	M	Gelatin	✓		✓	✓

4. Experimental results

4.1. Experimental data analysis

Matlab image toolbox (Matlab ®, MathWorks, Natick, MA) was used to process the videos from the side-viewing camera. Figures 6(a), 6(b), 6(c), 6(d) and 6(e) show one frame corresponding to experiments(A) to (E), respectively (Table 2). Each video was segmented when the forceps reached its lowest point. Typically, the gripper tip was slightly embedded into the gelatin, but the plane of the gelatin could not be determined. However, the video contained the forceps' reflection from the gelatin's surface. Since the distance that the gripper tip was embedded could not be measured directly, a template for both the forceps' image and the reflected forceps' image was prepared to estimate the location of both. In Fig. 6(a), 6(b), 6(c), 6(d) and 6(e), the red line was the segmented outline of the gripper with the red dot indicating the lowest point of the gripper and the blue line was the outline of the reflected gripper with the blue dot indicating the highest point of the reflection. We registered the blue and red outlines manually onto each picture. Half of the distance between the red and blue dots was used to estimate the gripper excursion depth in pixels into the gelatin substrate. The distance was then converted to microns by using the actual gripper length of 812 μm and its pixel length in each image to calculate the image scaling factor (γ(microns/pixel)) for each trial. Results are listed in Table 2 and described in section 4.2.

Figures 6(f), 6(i) and 6(j) show one retinal touch attempt for each of the respective experimental conditions (F) to (J). The gripper shape was segmented in red outline and the blue line indicated the blood vessel surface's location before the gripper touched it. Since there was no clear reflection from the goat retina, the blood vessel was the reference in calculating the excursion depth beyond the retinal surface. This distance was likewise calculated in microns from the forceps' tip (red dot) to the corresponding pre-touch blood vessel surface (blue dot). The experimental results are listed in Table 3 and described in detail in section 4.2. Representative side-viewing videos are presented for the (A) manual forceps touching gelatin (Media 2), (B) robot-assisted forceps touching gelatin (Media 3), (H) manual OCT-forceps touching retina (Media 4), and (I) robot-assisted OCT-forceps touching retina (Media 5).

Additional segmentations of the externally viewed motion of the gripper tips during one cycle of approach and retraction from the gelatin with manual surgical forceps (Fig. 6(k), (Media 2)) and with robot-assisted forceps (Fig. 6(l), (Media 3)) were performed. These videos were automatically segmented using the template-matching method. The red points represented instrument approach while the blue points represented instrumental retraction. Qualitatively, greater

#227007 - $15.00 USD Received 17 Nov 2014; accepted 22 Dec 2014; published 9 Jan 2015

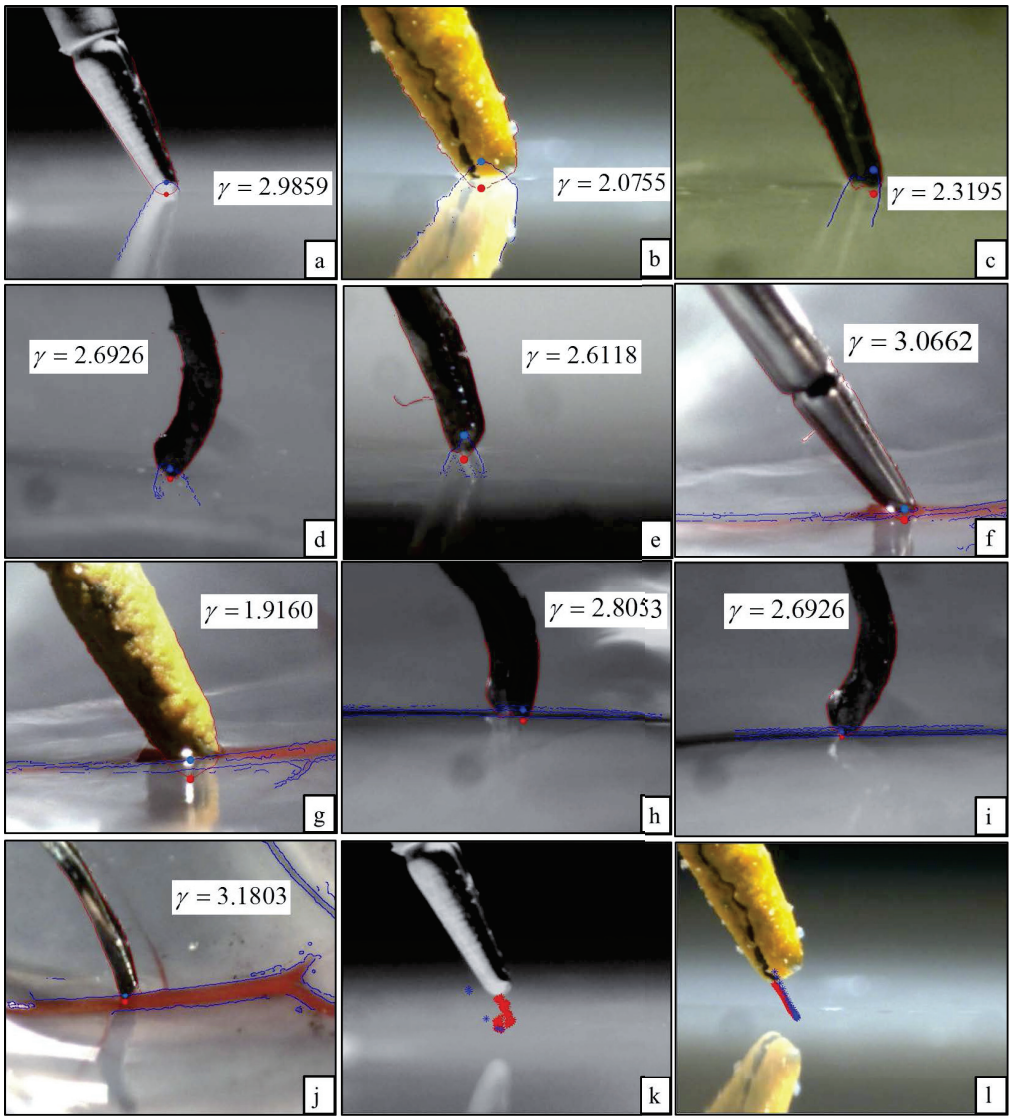

Fig. 6. Side-view image segmentation examples of the lowest point in one approaching attempt for each experimental condition. The red outline determined the lowest point of the gripper and the blue outline located the highest point of the reflected gripper. (a) through (j) are correlated with experiments (A) through (J). Corresponding videos are presented for the (a) manual forceps touching gelatin (Media 2), (b) robot-assisted forceps touching gelatin (Media 3), (h) manual OCT-forceps touching retina (Media 4), and (i) robot-assisted OCT-forceps touching retina (Media 5). (k, l) Examples of approaching(red) and retraction(blue) paths of the forceps' tips motion with (k) manual control (Media 2) and (l) robot-assisted control (Media 3) with obvious reduction in lateral movement with robot-assisted control.

#227007 - $15.00 USD Received 17 Nov 2014; accepted 22 Dec 2014; published 9 Jan 2015

lateral movements occurred with the manual forceps rather than with the robot-assisted forceps as expected. In addition, an example of real-time B-scan OCT imaging for four of the OCT-guided surface-touching conditions, including (C) manual B-scan OCT-forceps approaching gelatin retinal phantom (Fig. 7 (a), Media 6), (D) robot-assisted B-scan OCT-forceps approaching gelatin retinal phantom (Fig. 7 (b), Media 7), (H) manual B-scan OCT-forceps approaching a goat *ex vivo* retina (Fig. 7 (c), Media 8), and (I) robot-assisted B-scan OCT-forceps approaching a goat *ex vivo* retina (Fig. 7 (d), Media 9) are illustrated.

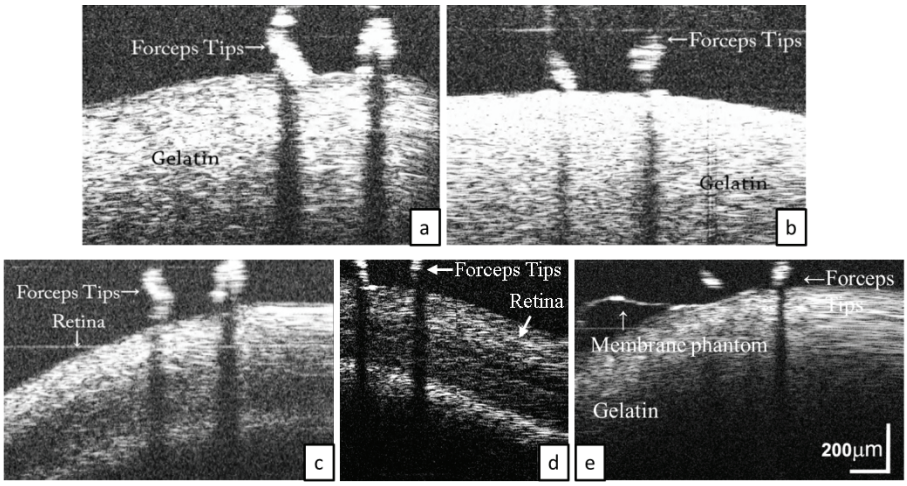

Fig. 7. Real-time B-scan OCT imaging examples for the OCT-guided conditions. (a) Manual B-scan OCT-forceps approaching gelatin phantom (Media 6). (b) Robot-assisted B-scan OCT-forceps approaching gelatin phantom (Media 7). (c) Manual B-scan OCT-forceps approaching goat *ex vivo* retina (Media 8). (d) Robot-assisted B-scan OCT-forceps approaching goat *ex vivo* retina (Media 9). (e) Real-time B-scan OCT imaging of peeling membrane phantom from gelatin (Media 10)

Peeling of the membrane phantom was possible with all 3 conditions (K) through (M). The number of attempts required for a successful membrane removal were recorded. The results of these experiments are listed in Table 4 and described in detail in section 4.2. An example of successful peeling with each of the conditions: (K) manual surgical forceps (Fig. 8 (a)), (L) robot-assisted forceps (Fig. 8 (b)), and (M) manual B-scan OCT-forceps with OCT-image side screen (Fig. 8 (c)) is illustrated (Fig. 8). An example of real-time B-scan OCT imaging of peeling membrane phantoms from the gelatin surface is presented (Fig. 7(e), Media 10) during condition (M) using the manual B-scan OCT-forceps with the OCT-image side screen.

4.2. Experimental data results

The results of approaching the gelatin phantom model are listed in Table 2. For total completion time, manual procedures were faster than robot-assisted procedures. This is because the speed of the robot was regulated to $1/50$ of the surgeon's hand speed for stability purposes. The last column provides the average depth $\pm$ standard deviation (S.D.) of the depth of excursion into the gelatin substrate. All distances were converted into microns. The non-parametric Kruskal-Wallis One Way Analysis of Variance (ANOVA) on Ranks demonstrated a statistically significant difference ($p < 0.001$) among the 5 groups. The smallest depth of penetrance of 13 ± 8 μm by the Tukey test ($p < 0.05$) was obtained when the surgeon used the robot with OCT feedback (D) (Fig. 9(a)). The comparisons among the groups are illustrated in Fig. 9(a)

#227007 - $15.00 USD Received 17 Nov 2014; accepted 22 Dec 2014; published 9 Jan 2015

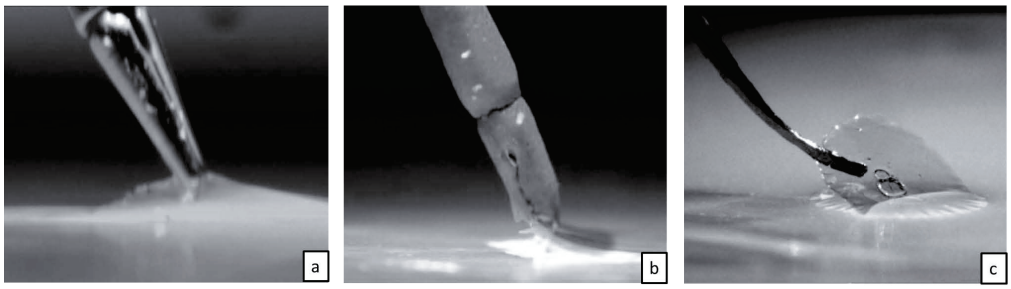

Fig. 8. Sid-view images of successful membrane phantom peelings from the gelatin surface. (a) Condition (K) using the manual surgical forceps. (b) Condition (L) using the robot-assisted forceps. (c) Condition (M) using the manual B-scan OCT-forceps with OCT-image side screen.

with significantly different ($p < 0.05$) comparisons identified. Figure 9(a) shows that there was no significant difference between the data acquired in experiments (A) and (B). This means that without OCT feedback, robotic assistance does not improve manual ability in depth judgment beyond the limitation of the surgical binocular microscope. When OCT feedback was introduced, manually holding the OCT-integrated forceps with the OCT image projected on a distant standard monitor did not have any improvement on the ability of performing the task due to the requirement of shifting gaze from the microscope to the distant screen. A small adjacent side screen as shown in Fig. 4(c) allowed the surgeon to limit eye movements for the OCT feedback and significantly improved the depth perception compared to the distant screen task (C), although it was not quite statistically superior over the manual forceps alone (24 μm vs 28 μm, $p > 0.05$, Tukey test). Finally, the robot-assisted OCT integrated forceps (D) produced the best results than any other experimental condition in touching the gelatin with minimal penetration into the substrate.

The results of approaching and touching the goat retina are listed in Table 3. Again, manual procedures were faster than robot-assisted procedures. The last column provides the average depth $\pm$ standard deviation (S.D.) of the depth of excursion into the retina. All distances were converted into microns. The non-parametric Kruskal-Wallis One Way Analysis of Variance (ANOVA) on Ranks demonstrated a statistically significant difference ($p < 0.001$) among the 5 groups. Comparisons among the groups are illustrated in Fig. 9(b) with significantly different ($p < 0.05$) values identified. The smallest depth of penetrance of 21 $\pm$ 11 μm again was obtained when integrated robot-assist and OCT feedback (I) was used (Fig. 9(b)), although it was not statistically different than the depth of 34 $\pm$ 17 μm produced by the manual integrated OCT-forceps with the small side view screen. Again, without OCT feedback, robotic assistance did not improve depth judgment significantly. OCT feedback reduced penetrance in the retinal touch task.

Demonstration that a first-generation prototype integrated OCT-forceps was capable of lifting a thin yet visible phantom membrane of Liquid Bandage upon gelatin was undertaken. Table 4 lists the membrane peeling results in experimental conditions manual (K), robot-assisted (L) and manual integrated OCT-forceps (M). The averages and standard deviations were plotted in Fig. 9(c). The nonparametric Kruskal-Wallis One Way Analysis of Variance (ANOVA) on Ranks ($p = 0.236$) indicated that the differences in the average values among the treatment groups were not statistically significantly different. The prototype integrated OCT-forceps was equally capable of peeling the membranes despite having smooth tips rather than commercial specialized tips with teeth. The total time for completing the task was also least with the integrated OCT-forceps (Table 4).

#227007 - $15.00 USD Received 17 Nov 2014; accepted 22 Dec 2014; published 9 Jan 2015

Besides the data documented in Tables 2-4 and Fig. 9, it was also observed that the robot-assisted manipulations were more stable than the manual manipulations. More lateral movement occurred with manual (Fig. 6(k)) than with robot-assisted (Fig. 6(l)) movements. Since the tasks designed in this study evaluated the accuracy in depth perception, the obvious stability advantage of the robot did not manifest itself in the results of this study.

Table 2. Results of approaching task on gelatin phantom model. M. = Manual; R. = Robotic; O. = OCT feedback; S.S. = Small Screen; S.D. = Standard Deviation

Exp. #	M.	R.	O.	M. + S.S.	# of Attempts	Total Completion time (s)	Average depth (S.D.) (μm)
A	✓				40	449	28(9)
B		✓			40	470	31(6)
C	✓		✓		40	171	36(16)
D		✓	✓		40	522	13(8)
E	✓		✓	✓	40	142	23(13)

Table 3. Results of approaching task on *ex vivo* retina. M. = Manual; R. = Robotic; O. = OCT feedback; S.S. = Small Screen; S.D. = Standard Deviation.

Exp. #	M.	R.	O.	M. + S.S.	# of Attempts	Total Completion time (s)	Average depth (S.D.) (μm)
F	✓				40	114	65(41)
G		✓			40	220	66(24)
H	✓		✓		40	162	50(27)
I		✓	✓		40	319	21(11)
J	✓		✓	✓	40	147	34(17)

Table 4. Results of membrane peeling task of liquid bandage on gelatin phantom. M. = Manual; R. = Robotic; O. = OCT feedback; S.S. = Small Screen; S.D. = Standard Deviation.

Exp. #	M.	R.	O.	M. + S.S.	# of Attempts	Total Completion time (s)	Fail to peel	Average (S.D.) attempts for successful peel
K	✓				85	1603	0	2.1 (2.5)
L		✓			85	1534	3	1.5 (0.9)
M	✓		✓	✓	85	1422	0	1.8 (1.2)

5. Discussions and conclusions

Optical coherence tomography imaging is valuable for identifying and diagnosing retinal disorders in the clinic. External microscope-mounted systems have demonstrated usefulness in examining retinal changes immediately following a surgical procedure in the operating room [9, 14–17, 43]. However, it would be most valuable to image critical portions of the operation in real-time with OCT cross-sectional imaging. Microscope-mounted OCT systems have limitations in that normal metallic surgical instruments cast absolute shadows upon the underlying targeted tissues [14–17] and investigators have reported difficulty in tracking the positions of moving surgical instruments within the eye [14–16].

A combined 23-gauge forward-imaging B-scan OCT-forceps was designed and developed for manual use or robotic-assisted integration for pre-clinical retinal surgery. Unlike other minia-

#227007 - $15.00 USD Received 17 Nov 2014; accepted 22 Dec 2014; published 9 Jan 2015

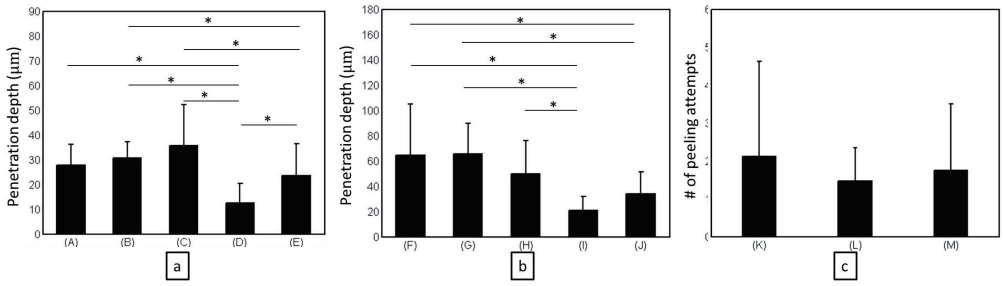

Fig. 9. Averages and standard deviations of the data with significantly different groups marked with * ($p < 0.05$). The x-axis labels the experimental condition as described in Table 1. The y-axis indicates the means and standard deviations of the measurements. (a) The approaching task to the gelatin phantom model (A to E); (b) The approaching task to the *ex vivo* goat retina (F to J); (c) The membrane peeling task on the gelatin phantom model (K to M).

ture forward-imaging probes, this probe has an internal scanning system so it can be held steady rather than moving the entire probe back-and forth to produce a two-dimensional B-scan image. The size of the OCT-forceps probe will permit passage through the current 23-gauge ports used in vitrectomy procedures. An advantage of an intraocular OCT probe is that it overcomes some of the problems associated with an external microscope-mounted OCT system. The probe bypasses the corneal and lenticular opacities that will degrade an OCT image. The intraocular probe can quickly be positioned and aimed at the areas of interest for imaging inspection. Co-planar integration of the forward-imaging B-scan probe with a surgical instrument permits constant tracking of the instrument tip without needing a tracking device embedded in the instrument. In addition, the instrument's position and approach to the tissue is provided with real-time feedback without requiring real-time layer segmentation or spatial compounding unless semi-automatic robotic control is desired. Finally, placing the OCT imaging probe internal to the surgical tool improves the view of the desired target by reducing instrument shadowing. A series of experimental conditions to evaluate the potential benefits of using robotic assistance and OCT-feedback was performed. Two benchmarking tasks included touching a gelatin phantom surface and an *ex vivo* goat retinal surface while avoiding penetration into the substrates. They were performed under five different experimental conditions, which included manual and robot-assisted performance with and without 23-gauge forward-imaging B-scan OCT feedback to the user. Compared to previous robotic works [36], our study focused on evaluating control of depth penetration instead of the lateral steadiness superiority that is expected with robotic systems.

The results demonstrated that when operating through the sclerotomy constraints of the phantom eye model, the robot alone did not improve the surgeon's depth judgment in touching the gelatin phantom or the *ex vivo* goat retinal surface. When the OCT feedback was introduced, manually holding the OCT probe tool initially worsened performance, because the surgeon had to shift his vision between the surgical microscope binoculars and the distant large OCT image screen. Addition of a small side-view monitor next to the microscope binoculars for real-time OCT image display greatly improved the manual performance of the approaching tasks which emphasized the need for improved monitors for intraoperative OCT viewing. Tao, *et al.* recently described projecting an OCT image through a surgical microscope ocular which may even further improve performance [10]. When the real-time feedback from the 23-gauge OCT-forceps was combined with robot-assist control, the surgeon's performance was dramatically improved compared to the other experimental conditions. This is consistent with prior robot-

#227007 - $15.00 USD Received 17 Nov 2014; accepted 22 Dec 2014; published 9 Jan 2015

assisted studies which demonstrated improved microsurgical performance by significantly reducing hand tremors [27, 28, 36]. Similar reduction of lateral drift with the approach tasks was observed with the robot-assist forceps compared to the manual forceps as depicted in Fig. 6(k) and 6(l).

The membrane peeling task demonstrated that the first-generation integrated OCT-forceps prototype was equally capable of peeling membrane phantoms despite having smooth tips compared to the other forceps designed with special tips for grasping membrane edges. Additional system improvements will be to optimize the tips of the forceps for grasping thin membranes. In addition, an ideal future phantom model would contain a standardized thin membrane barely visible *en face* through the surgical microscope to better compare the capabilities of the system with and without both real-time OCT imaging and robotic assistance. Although a cadaver animal retina unfortunately has variable retinal thickness and nonuniform responses to artificial membrane placement to preclude quantitative comparisons of membrane peeling, it was useful for demonstrating initial preclinical feasibility. A vitrectomized living ocular model will be the next step in the preclinical evaluation of the intraocular OCT-forceps probe. Rotational movements of the forceps will be scaled in future experiments to increase mobility. Algorithms as developed by Huang and Kang [44] will minimize reference fixed pattern artifact and saturation artifacts. In addition, an OCT engine with faster real-time acquisition rate should improve the quality.

In conclusion, real-time intraocular B-scan OCT visualization of tissue microstructure and feedback of surgical maneuvers is a desired ophthalmic feature. An intraocular 23-gauge B-mode forward-imaging co-planar OCT-forceps along with coupling connectors and algorithms to a unique ophthalmic surgical robotic system were developed. Real-time manual OCT-forceps feedback with a small side monitor and real-time robot-assisted OCT-forceps feedback improved depth perception accuracy. Future studies will examine whether more intricate subretinal and retinal vascular maneuvers can be performed with the intraocular robot-assisted OCT-forceps to permit the improvement of current vitreoretinal procedures as well as the development of new techniques.

Acknowledgments

This research was funded from Vanderbilt discovery grant #422-999-0095, Vanderbilt ViSE fellowship #433-999-4000, NIH 1R21EY019752, Joseph Ellis Family Research Fund, William Black Research Fund, Vanderbilt Vision Research Center P30EY008126, and Unrestricted Grant from Research to Prevent Blindness, Inc., N.Y. to the Vanderbilt Eye Institute. The authors would like to thank Amy Nunnally for the goat eyes.